A WAFER-INTEGRATED ARRAY OF MICROMACHINED ELECTROSTATICALLY-DRIVEN ULTRASONIC RESONATORS FOR MICROFLUIDIC APPLICATIONS

B. A. Parviz, T. -K. Chou, C. Zhang, K. Najafi, M. O. Muller*, L. P. Bernal*, P. Washabaugh*
Center for Integrated MicroSystems,
*Aerospace Engineering Department,
University of Michigan
1301 Beal Ave., Ann Arbor, MI 48109-2122 USA

ABSTRACT

A distributed micromachined ultrasound source is presented. Electrostatic actuators operating at frequencies exceeding 100kHz are coupled to a Helmholtz resonator in order to achieve high output velocities. They consist of a 1200μmx1200μmx1.36μm composite diaphragm, a perforated P++ backplate and a 3μm air gap. The actuators cover the entire surface of a 4" wafer and are grouped in four individually addressable quadrants. A robust micromachining technology with >80% yield, employing anodic glass-silicon bonding, dissolved wafer process and advance deep silicon etching has been developed for fabrication of the actuator array. The dynamic behavior of the diaphragm was studied using laser interferometry, and operation was verified at 96kHz by acoustic measurement.

INTRODUCTION

Intense ultrasound beams have numerous applications in various fields ranging from medical imaging to non-destructive material testing or distance measurement. A micro ultrasound source can be used for local initiation of chemical reactions, metal electroplating [1], fluid atomization, localized bacteriocidal action and biological manipulation or genetic mutation. At high intensities, the ultrasound source can generate acoustic streaming and thus transfer considerable momentum to the medium [2]. In this case, the resultant fluid stream can be used for propulsion or be employed as part of a micro cooling system or a micro pump [3].

In this paper a distributed micromachined ultrasound source is presented. The source consist of 992 resonators which cover the entire surface of a 4" wafer. The wafer is grouped in four quadrants, each individually addressable. The next section describes the basic principle of operation for each resonator. The following section details the fabrication process, nd then results are presented. Characterization data is gathered by acoustic measurements and laser interferometry coupled with a high speed CCD camera system.

PRINCIPLE OF OPERATION

An electrostatically driven diaphragm that actuates air in the cavity of a Helmholtz resonator forms the heart of the system. Figure 1 shows a cross section of a Helmholtz resonator unit:

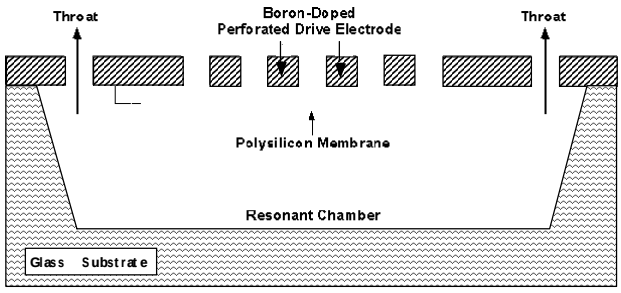

Figure 1: Cross section of a Helmholtz resonator unit.

The diaphragm is made of boron-doped polysilicon and dielectric isolation layers of silicon dioxide and silicon nitride. The stress of the diaphragm is tailored to match the resonance frequency of the Helmholtz resonator and the diaphragm, and thus provide good power delivery efficiency. The diaphragm is separated from a 15μm-thick perforated backplate by a 3μm gap. The backplate is made of boron-doped single-crystal silicon and contains a pattern of holes for reducing air damping. The effect of the size of these holes is discussed in a later section. A deep cavity formed in a glass substrate faces the diaphragm from one side. Two curved throats connect the interior of the cavity to the out side world.

When an alternating voltage is applied across the actuator gap, the diaphragm starts to oscillate. This motion in turn creates an acoustic field inside the cavity. The initial velocity generated in the cavity is amplified by the Helmholtz resonator [3,4] and upon exit from the throat, contingent upon having a sufficiently high velocity, the acoustic field creates a jet stream [5]. Figure 2 shows the calculated pressure fluctuation amplitude in the cavity as a function of the actuation frequency. Here, it is assumed that upon application of voltage, the diaphragm fully collapses against the backplate.

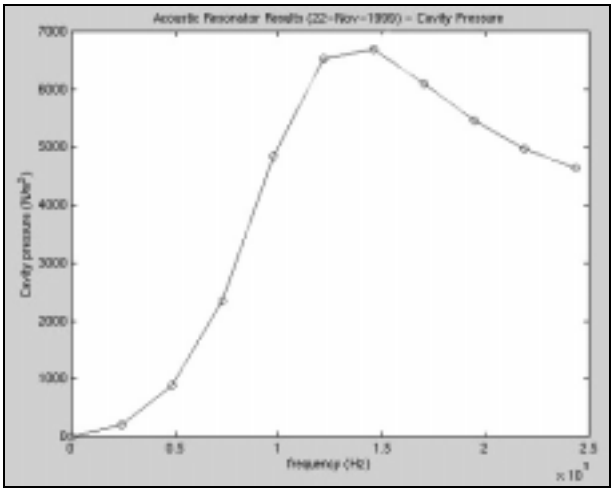

Figure 2: Calculated cavity pressure fluctuations vs. actuation frequency

This amplitude reaches 6700Pa at the resonance frequency. This is a very large pressure to overcome for the electrostatic actuator and thus 130V is needed for full operation at resonance. Figure 3, shows the calculated output flow velocity based on compressible and incompressible flow models.

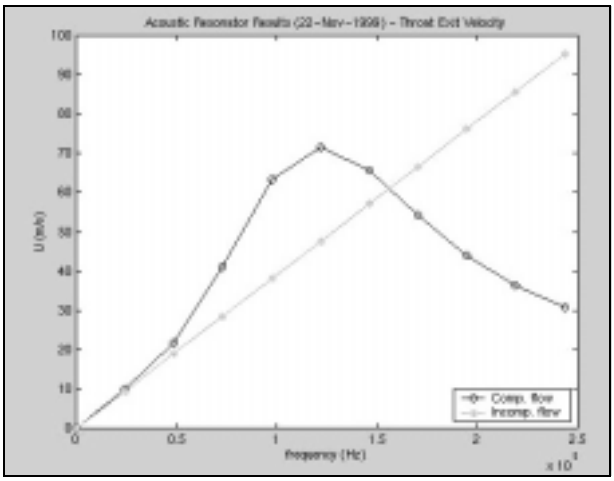

Figure 3: Calculated air velocity at the throat exit vs. input voltage frequency. Compressible and incompressible models are compared.

The compressible flow model predicts a large deviation around the resonance frequency and velocities as high as 70m/s which is enough for initiation of acoustic streaming.

The resonators are placed in a hexagonal fashion around a circular area, which could eventually be used as a part of a jet nozzle (not discussed in this paper). Each resonator is shared between two circular areas with each throat supporting a nearby circle. Figure 4 shows the top view of the layout of a hexagonal unit.

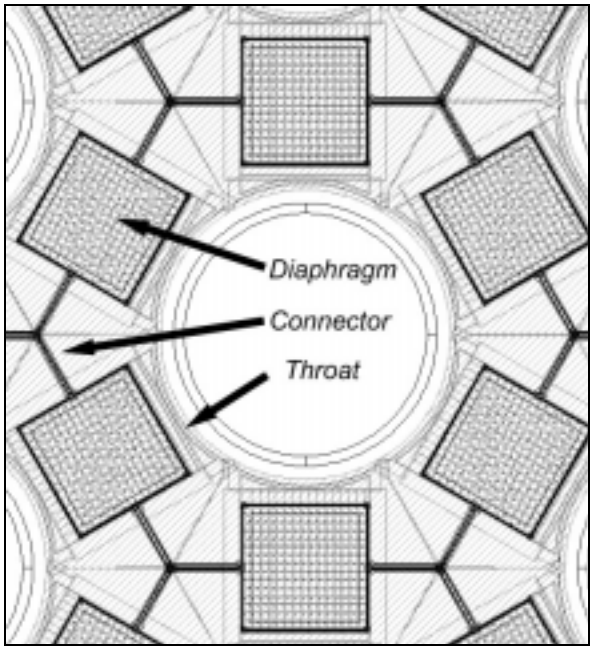

Figure 4: top view; hexagonal unit consists of six resonators surrounding an ejector area. Parts of neighboring units are also shown.

The wafer is divided in to four equal quadrants. Each quadrant contains 70 hexagonal unit cells which yields a total of 992 resonators covering the wafer surface. All the resonators in a quadrant operate in parallel and each quadrant can be actuated independently. Table I summarizes the characteristics of individual resonators.

Table I: Resonator characteristics

PARAMETER	VALUE
Diaphragm Dimensions	1200µm x1200µm x1.36µm
Diaphragm Res. Freq.	112.79 kHz
Helmholtz Res. Freq.	121.7 kHz
Res. Cavity Dimensions	30µm x1350µm x1730µm
Throat Dimensions	15µm x 15µm x 1406µm
Perforation Hole Size	40µm x 40µm x 15µm
Actuator Gap	3µm
Max. Cavity Pressure	6700 Pa

FABRICATION PROCESS

A wafer-level fabrication process has been developed for construction of the device. The process is capable of creating MEMS devices covering the entire surface of a 4" wafer and has proved to be very robust and possesses high yield (>80%). The structure is made of two wafers. The first one, a silicon wafer, contains the main parts for the electrostatic actuator such as the diaphragm and the perforated backplate. It also contains connectors, which link resonators in each quadrant. The second wafer, a #7740 Pyrex glass wafer, contains the resonance cavity and trenches for embedded connector lines. Figure 5 shows the summary of the fabrication process.

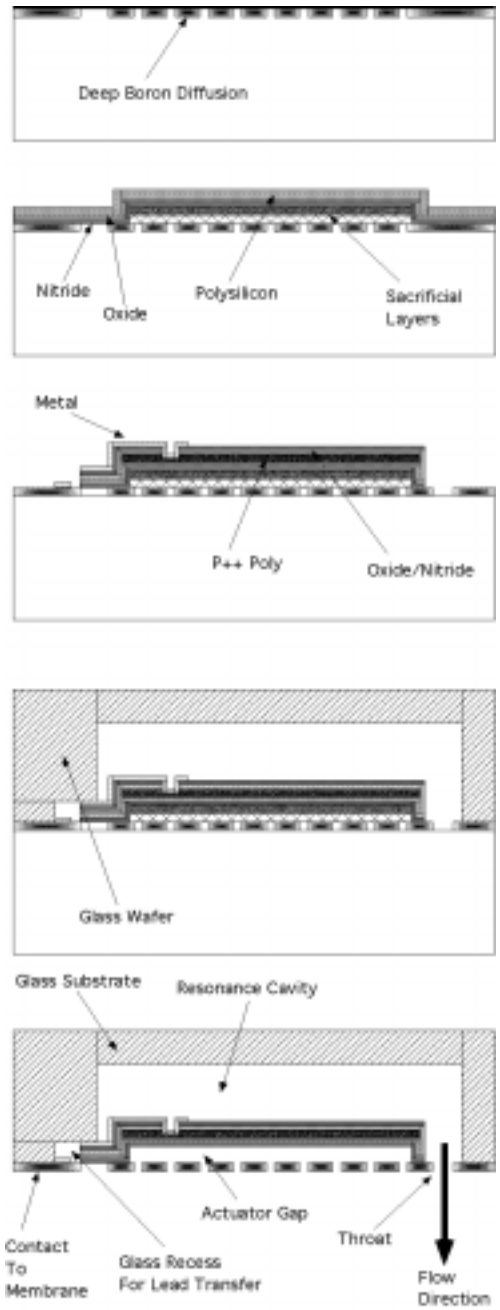

Figure 5: Simplified cross section of the process flow.

The process on the silicon wafer starts with thermal growth and patterning of a silicon dioxide layer (1μm) which acts as a diffusion mask. Then a 16hr deep boron diffusion step is performed to define the perforated backplate and separation areas between devices. The lower limit on the size of the holes in the backplate is determined here by diffusion of boron atoms under the oxide mask. In the first iteration of the device the holes were 40μmx40μm squares with 40μm spacing. In the second design iteration, it was determined that smaller hole sizes and spacing were required. These dimensions were not possible to fabricate because of the significant under diffusion of boron. Thus the process was slightly modified to accommodate the new geometry. In the modified process, a blanket boron diffusion substituted the patterned diffusion as the first step and damping holes were defined by deep etching of silicon (15.6μm) after the first release step. This way, 5μm holes with 5μm spacing were created in the back plate.

After removal of the masking oxide, a sacrificial layer consisting of silicon dioxide (1μm) and polysilicon (2μm) is deposited. Next, a composite diaphragm is formed using a heavily boron-doped polysilicon layer (0.8μm), sandwiched between a composite of silicon dioxide (0.15μm on each side) and silicon nitride (0.13μm on each side) layers. The square shaped diaphragm is 1200μmx1200μmx1.36μm. The composite residual stress in the diaphragm is +91.9MPa which sets the resonance frequency of the structure at 112.79kHz. Control of the residual stress of the diaphragm is crucial in ensuring the structural integrity and proper functionality of the device. Diaphragms with higher residual stress levels (380MPa and 180MPa) were fabricated by using only dielectric layers. All the high stress diaphragms ruptured after the final release. After diaphragm layer deposition and patterning, contact holes are etched in the device by RIE and Cr/Au (200Å/8000Å) connectors are sputtered and patterned. The patterns in the glass wafer are formed by using sputtered Cr/Au masks and wet etching in a HF:HNO_3 solution. The cavity depth is 30μm and the trench depth is kept at • 7μm. Trenches are used to support gold interconnects and create a flat surface for bonding.

After both the silicon and glass wafers are completed, they are bonded anodically at 360°C by application of 1000V bias. The bonding is performed at a lower temperature to avoid eutectic flow of gold over polysilicon contacts. After bonding, the un-doped silicon is dissolved away from the backside by performing a wet etch in EDP and subsequently the sacrificial silicon dioxide layer is etched in BHF and finally the device is released by an EDP step to remove the sacrificial polysilicon. For devices with 5μm damping reduction holes, after the first EDP step, theholes are etched by deep silicon etching using an ICP source. This is followed by etching of the sacrificial layers and release of the structure.

FABRICATION RESULTS

A number of wafers have been fabricated. One of the challenges in the fabrication process was formation of deep cavities in the glass substrate. Various techniques were investigated to form the recess and the cavity, and finally a controlled wet etch was used to create the desired structure. Surface roughness of the glass wafer was found to be the main factor in determining the lateral etch front progress. The glass wafers used in this experiment had surface roughness of 50Å. The lateral etch was accounted for in the mask design.

Figure 6 shows an SEM picture of one of the hexagonal unit cells. The silicon part has been separated from glass to provide a clear view of the device. The six resonators surrounding the ejector area and connector lines can be observed in the picture. Figure 7 shows a close up of a resonator; the diaphragm is partially removed to expose the perforation pattern in the back plate. One of the two curved throats connecting the resonance cavity to the outside can be seen next to the damping holes at the top of the picture. Figure 8 shows a completed wafer covered with resonators. The four quadrants can be recognized in this photograph. As described in the next section, to reduce damping in the perforated back plate, the 40μm holes were substituted by 5μm holes. Figure 9 shows part of a perforated back plate covered with damping holes next to the curved throat. In the modified design, each resonator has more than 14,000 damping holes which amounts to more than 1,400,000 damping holes for the four quadrant system.

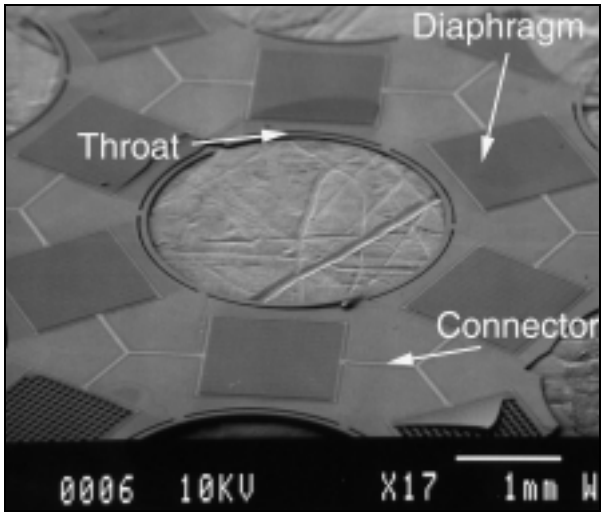

Figure 6: SEM picture of a unit cell showing six resonators around an ejector opening

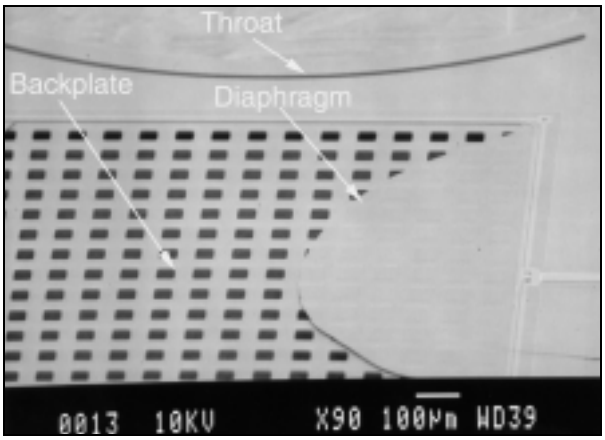

Figure 7: A close up of a partially removed diaphragm, perforated backplate and part of one of the throats supporting a resonator.

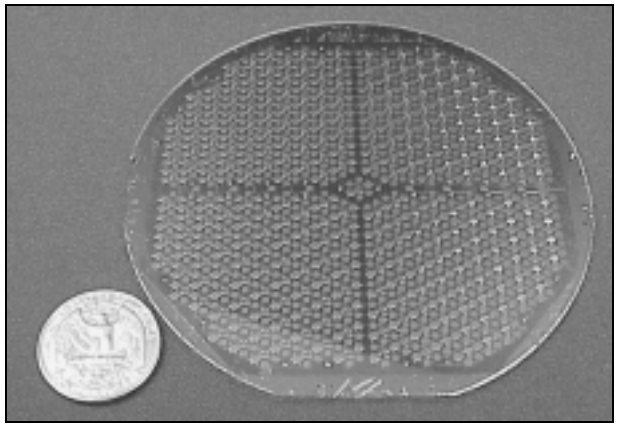
Figure 8: A completed wafer covered with resonators next to a US quarter. Four quadrants and individual devices can be recognized here.

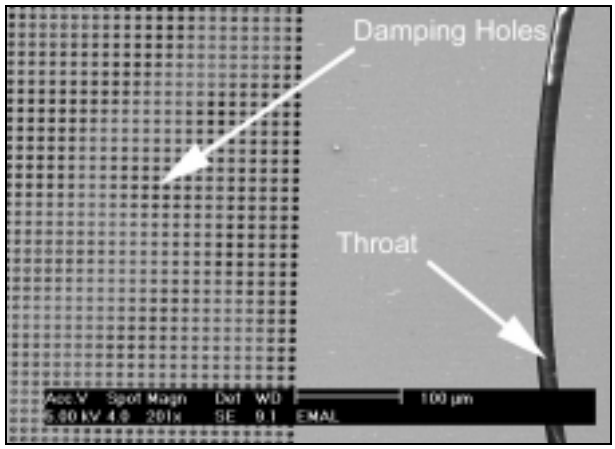

Figure 9: Top view of 5μm damping holes and part of the curved throat opening.

CHARACTERIZATION RESULTS

A number of electrical, optical and acoustic tests were conducted on the fabricated devices to characterize the performance of the electrostatic actuators and measure the acoustic output.

Laser Interferometry

The dynamic behavior of the actuators was investigated by using interference images of the diaphragm illuminated by a YAG laser, and a high speed CCD camera, as illustrated in Fig. 10. The trigger for the CCD camera was synchronized to the driving signal in order to trace the motion of the structure in one cycle. In order to avoid charge build-up in the silicon nitride layer adjacent to the perforated back plate, a customized waveform was applied to drive the actuators. By altering the polarity of the applied pulse at each cycle the net charge build-up was decreased and long-term shifts in the device behavior reduced. Full collapse of the diaphragms was verified at frequencies as high as 17kHz. Figure 11 shows three consecutive images acquired from the laser interferometer system. The input

signal was a series of pulses (60µs on,40µs off) with the amplitude alternating between +62V and -62V in every other cycle. Figure 1aa, shows the diaphragm at rest (0µs from the start of the pulse), Figure 11b shows the diaphragm during the rise time (20µs). By counting the number of fringes the total deflection can be determined. Each fringe represents 0.244µm of displacement. Figure 11c shows the full collapse of the diaphragm (60µs).

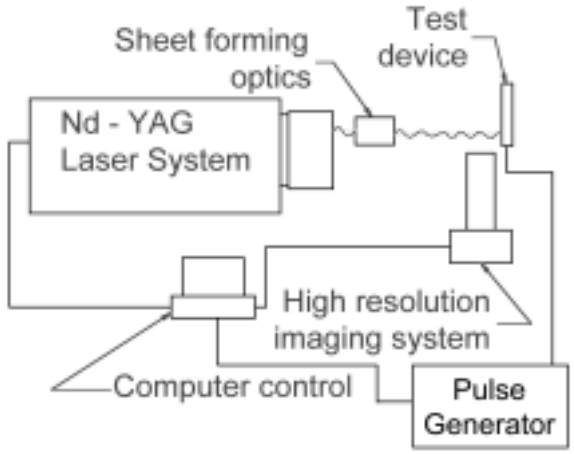

Figure 10: Schematic of the laser interferometry setup.

Acoustic Measurements

It was observed that the lower limit on the collapse time of the diaphragm was about 50µs for 40µm damping holes. This problem was associated with excessive damping in the area between the back plate and the diaphragm. In order to alleviate the problem, a new set of damping reduction holes were designed and fabricated as shown in Figure 9. Figure 12 shows a comparison between the calculated average damping pressure exerted on the back plate as a function of hole size. Here, it is assumed that the hole spacing is equal to the hole size and the entire back plate is covered by them. Also the flow has been assumed to be laminar and incompressible[6].

This confirms a significant reduction in damping by using the 5µm holes. The new device could generate ultrasonic output at frequencies as high as 96KHz and beyond Since all the microphones used in this experiment had frequency responses rolling off at 20kHz, there is a significant signal loss associated with the high frequency acoustic measurements and the actual output signal is expected to have a larger value. Figure 13 shows the acoustic output at a distance of about 3cm measured from two quadrants driven by a 48kHz, 28V signal.

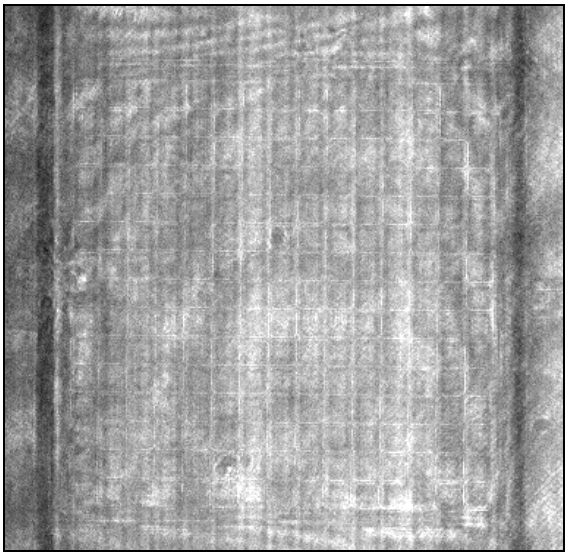

(a): Diaphragm at rest, no deflection

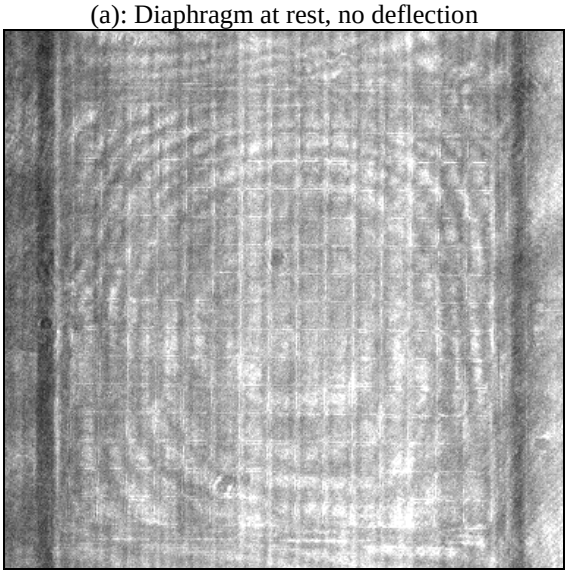

(b): Diaphragm at half deflection (• 1.8µm)

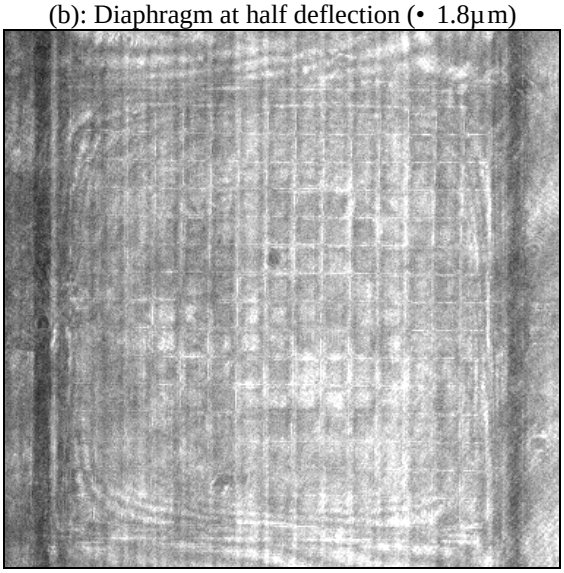

(c): Diaphragm, at full deflection (3µm)

Fig. 11: Sequence of photographs showing diaphragm position after 0,20 and 60µsec (see text)

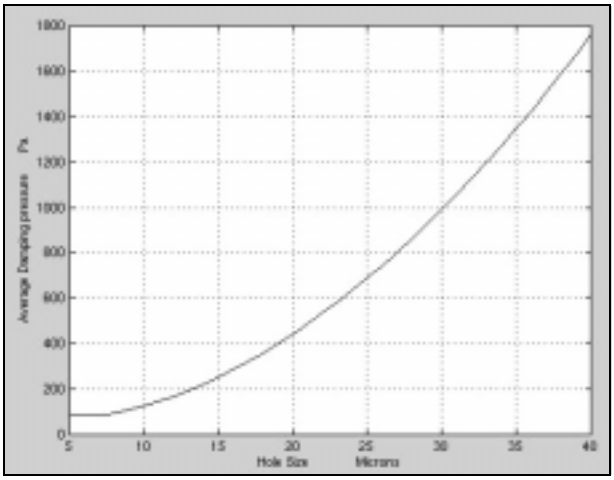

Figure 12: Calculated average damping pressure as a function of perforation size (120kHz operation)

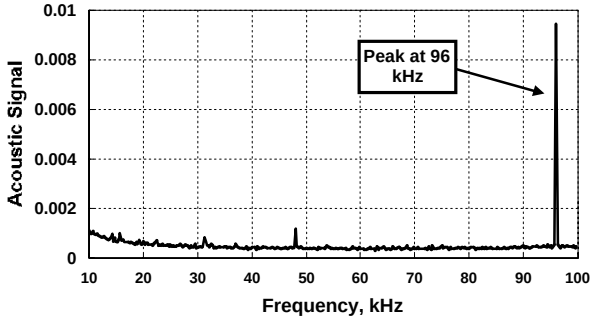

Figure 13: Measured acoustic spectrum of the output generated by two quadrants of the wafer.

As expected, the main measured output peak is observed at 96kHz. Figure 14 shows the harmonics generated by the same device when actuated at audio frequencies (3kHz, 45V). It is notable that the device can be clearly heard from the distance of a few meters. The harmonics are generated mainly because of the square function relationship between the applied voltage and the resultant pressure in the electrostatic actuator. Also, since the diaphragm is operated in collapse mode in a nonlinear fashion, extra harmonics are generated at the output. These figures clearly show the operation of the device at very high frequencies.

CONCLUSIONS

A novel distributed micro ultrasonic source has been designed and fabricated. The ultrasound source is fabricated using a robust micromachining technology which is suitable for large area MEMS fabrication with high yield. The functionality of the source was investigated by using high speed laser interference imaging. The imaging duration was limited to • 5µs; however, if higher power lasers are used this time interval can be reduced. Air damping, dielectric charge build-up and humidity effects were important parameters influencing the functionality of the device. Air damping models based on simple incompressible laminar flow assumption in the back plate holes did not match experimental results and thus more detailed modeling is needed to better describe the device behavior at higher frequencies.

Ultrasonic signal outputs were measured at frequencies as high as 96kHz. Because of the non-linear nature of the device operation, the source creates strong higher order harmonics and thus is not suitable for single tone applications; however, at high frequencies (~100kHz) a jet stream is expected to form at the exit throat of the resonators. Taking advantage of this jet stream could be the main use of the device in micro fluidics applications.

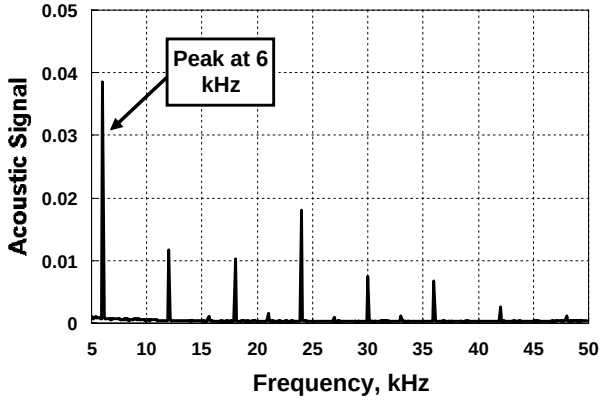

Figure 14: Measured higher harmonics generated by acoustic actuation at 3kHz, 28V

ACKNOWLEDGMENTS

The authors thank Dr. Abhi Chavan for stimulating discussions and guidance for development of the anodic bonding process, and Mr. Hsiao Chen for help with Deep Silicon Etching. This work was supported by DARPA under contract # N00019-98-K-0111.

REFERENCES

[1] B. Brown and J. E. Goodman, "High-Intensity Ultrasonics", p213, London ILIFFE Books Ltd,1965

[2] J. Lighthill, "Acoustic Streaming", J. Sound and Vibration, V61, No3, pp.391-418, 1978

[3] B. A. Parviz, L. P. Bernal and K. Najafi, " A Micromachined Helmholtz Resonator For Generation Of Microjet Flows", Proc. Transducers '99, pp.1788-1791, Sendai, Japan, June 1999

[4] R. C. Chanaud, "Effects of geometry on the resonance frequency of Helmholtz resonator", J. Sound and Vibration, V178, N3, pp. 337-348, 1994

[5] D. J. Coe, et al, "Addressable micromachined jet arrays", Proc. transducers '95, pp.329-332, Stockholm, Sweden, June 1995

[6] Z. Skvor, "On the acoustical resistance due to viscous losses in the air gap of electrostatic transducers", Acustica, pp. 295-299, V19, 1967/68